4

RESULTS

This chapter focuses on the main experimental results of this work. It begins with the growth of the CoO ultrathin films on the Ag(001) single crystal, then describing macroscopic structural and magnetic properties of the oxide film or the Fe/CoO bilayers and finally arriving at the microscopic properties of the films and interfaces studied by the spectroscopic and microscopy methods described previously.

Contents

4.1   Growth and structural characterization

A properly-oriented Ag(001) crystal with a miscut angle smaller than 0.2° exhibits after several cycles of sputtering and annealing, a sharp (1x1) LEED pattern [Fig. 4.1 (a)].

The CoO deposition technique was already presented in Chapter 3. Films of different thicknesses (up to 13 ML), were deposited each of them showing a LEED pattern that resembles the Ag pattern. Figure 4.1 presents the pattern recorded for 3, 6, and 9 ML of CoO/Ag(001). This result proves that the CoO adopts the crystal structure of the substrate and formation of films with a different crystallographic orientation [44] can be excluded.
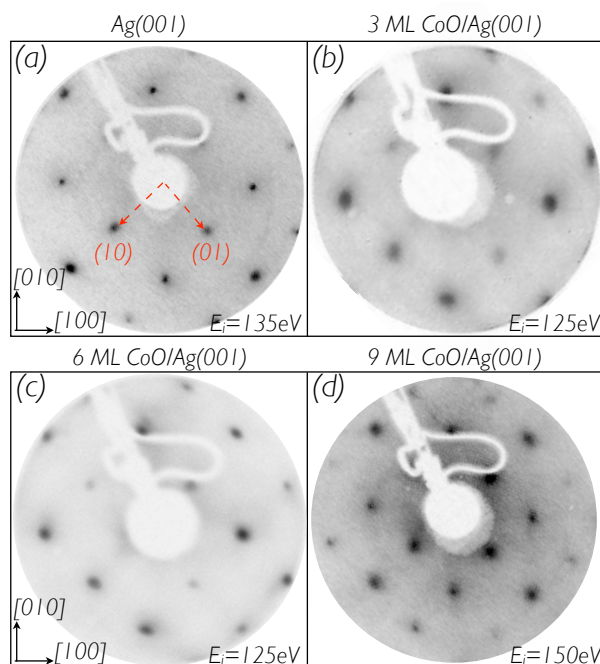

Figure 4.1: (a) LEED patterns of Ag(001) and different thicknesses of CoO grown on top (b, c, d). Strong and sharp reflections are present for the whole range of studied thicknesses indicating an ordered growth mode. The parameters used for deposition had been found varying the temperature of the sample and the annealing temperature and duration : T = 470 K, p_{O_2} = 2.0^{-6} mbar, T_{anneal} = 750–780 K. Electron energies and main crystallographic directions are indicated.

The most important parameters for the CoO growth are: the substrate temperature, oxygen pressure and substrate smoothness. Too low sample temperature can lead to precursor formation – islands with different CoO arrangement and structure and thus no long range order is present, the LEED patterns show either no spots or only broad spots [Fig. 4.2 (a)]. After the substrate temperature is increased, a big improvement in the spot quality is visible. But the best pattern (*i.e.* smooth surface) can only be obtained performing a post-annealing of the CoO for 30 min in oxygen atmosphere (pressure is not higher than the one used for deposition). Concluding, in the first step of growth one
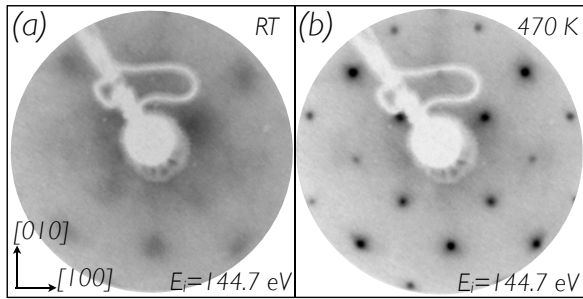
Figure 4.2: (a) shows the room temperature prepared film followed by no annealing. Higher substrate temperature during growth and post annealing leads to a proper oxide surface (b). Patterns presented here correspond to a 10 ML CoO/ Ag(001) and the annealing temperature and pressure was T_{anneal} = 750 K and p_{O_2} = 2.0×10^{-6} mbar, respectively.

has to be sure that no precursor islands are formed at the surface. At the same time, the right amount of oxygen for a proper oxidation of the Co has to be provided. Influence of the annealing temperature can be directly seen in the image Fig. 4.2 (b). The images are recorded at the same sample position and energy before and after annealing the sample at 750 K, for 30 minutes at p_{O_2} = 10^{-6} mbar oxygen pressure.

A lower oxygen pressure during deposition or a higher Co deposition rate at the same pressure leads to wrong type of oxide formation and LEED patterns with broad spots.

For a more complete overview on the growth of CoO on Ag(001), STM experiments were also carried out. A 8.3 ML–thick CoO film was prepared as presented above. The sample temperature during deposition was 450 K. Figure 4.3 presents two images recorded at room temperature before and after annealing of the sample. The improvement of the surface roughness in the case of the annealed sample is clearly visible . The line profiles show that for a non-annealed sample, the CoO is forming high islands. Horizontal areas with different contrast in the bottom image are due to the possible bonding/unbonding of an oxygen atom to the STM tip.

The Fe layer deposition and structure was checked by means of LEED. The two images in Fig. 4.4 show the LEED pattern for a layer of CoO with a thickness of 10 ML covered with 5 ML and 8 ML of Fe, respectively. The epitaxial growth of Fe on top of CoO is evident. Here the "as-grown" structure is
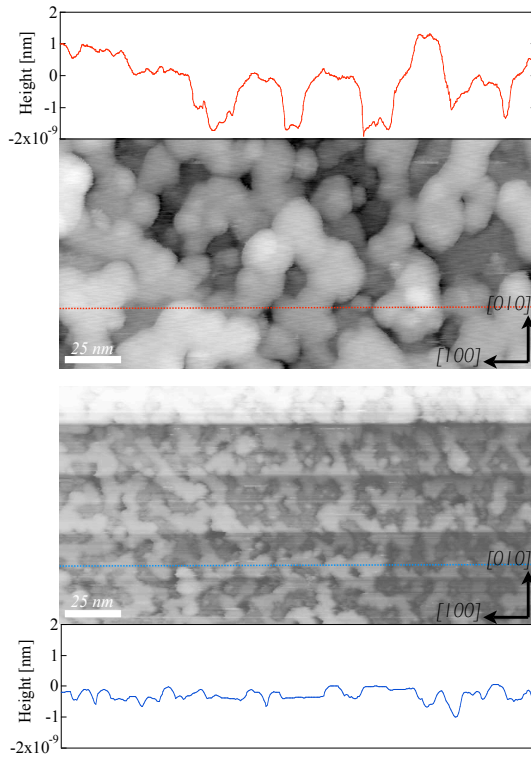
Figure 4.3: STM images for a 8.3 ML CoO film deposited on Ag(001). The upper image is recorded before annealing the sample. Large islands are in this case visible in the profile line. After annealing at 700 K, a clear improvement in the surface smoothness is evident. Horizontal line scans depict the roughness of the CoO surface before (top) and after (bottom) annealing of film. ($V_T = 2.5$ V and $I_T = 0.5$ nA)

recorded since no annealing of the Fe layer on top of the CoO was performed to avoid thermal diffusion of the oxygen from the CoO into the Fe layer.

A thermal treatment helps to improve the quality of the Fe film (as it does with oxides films CoO, NiO [60], MgO [104] or metallic Fe, Ni, Co, Mn [105, 14, 66] films) but in our case, the annealing temperature would probably also influence the structure of the Fe/CoO interface. Therefore, in this work, annealing was performed only on the CoO film prior to deposition of Fe. Furthermore, the Fe layer was deposited on the previously annealed CoO only at room temperature, after the oxide film was thermalized and the pressure in the preparation chamber reached 10^{-10} mbar after pumping out all the oxygen used
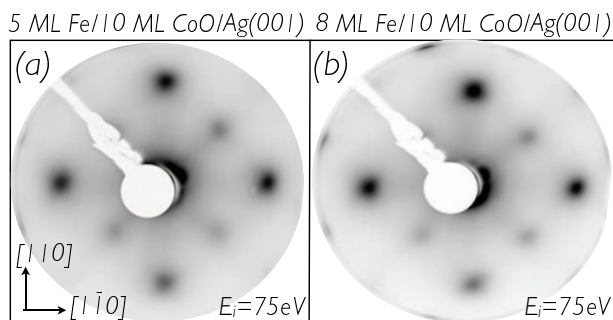

Figure 4.4: LEED pattern for 5 ML Fe/10 ML CoO/Ag(001) (a) and 8 ML Fe/10 ML CoO/Ag(001) (b) recorded at room temperature.
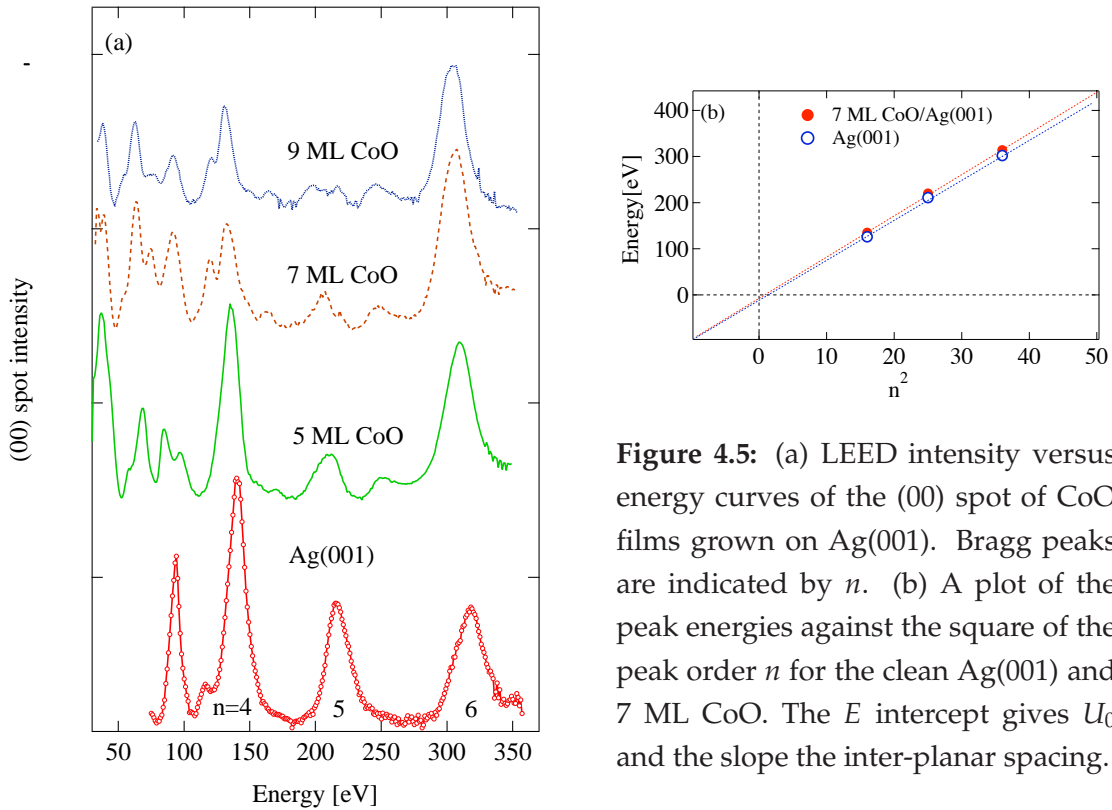
Figure 4.5: (a) LEED intensity versus energy curves of the (00) spot of CoO films grown on Ag(001). Bragg peaks are indicated by n. (b) A plot of the peak energies against the square of the peak order n for the clean Ag(001) and 7 ML CoO. The E intercept gives U_0 and the slope the inter-planar spacing.

for the oxide layer deposition.

After presenting an overview on the in-plane structure of the films, we now turn our attention to the structure along the surface normal. As explained before, LEED *I(E)* curves can be used to extract the averaged vertical interlayer spacing *via* a simple kinematic analysis of the (00) spot intensity.

During the LEED *I(E)* data acquisition, the sample was aligned at an incidence angle of 5° to the surface normal. The Ag (001) direction was fixed parallel to the plane of incidence. The voltage of the electron gun was increasing in steps of 0.2 eV. The software used to record the curves was set to integrate the (00) spot intensity over a pre-set area. At the same time, the intensity of a "dark" area was recorded in the same way. This provided the background used to normalize the *I(E)* curves.

Figure 4.5 (a) shows the LEED *I(E)* curves recorded for different CoO thicknesses deposited on Ag(001): 0 ML (clean Ag surface), 5, 7, and 9 ML CoO. The different peaks that arise from different single scattering events correspond to the single-scattering Bragg peaks of order $n = 4$, 5, and 6. In Fig. 4.5, a shift of
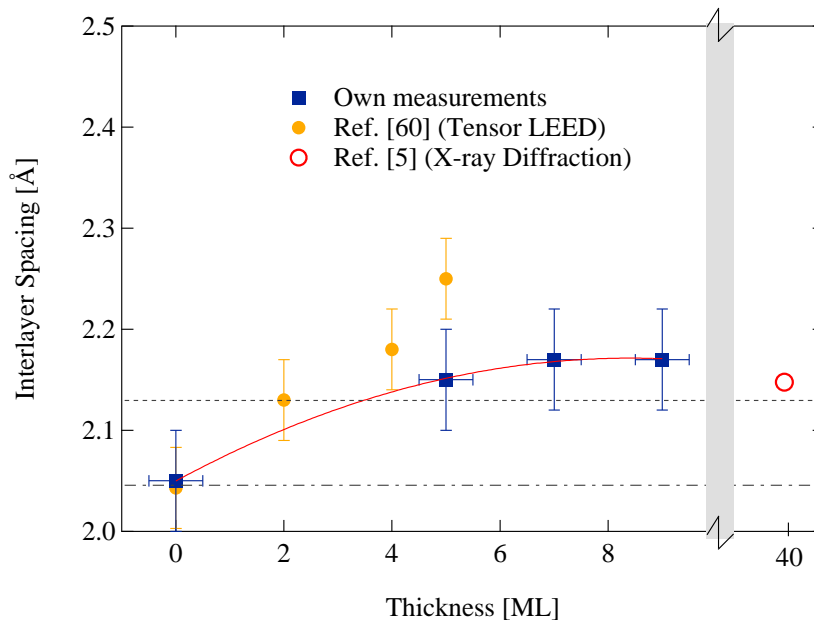
Figure 4.6: Summary of results concerning the vertical layer spacing for CoO/Ag(001). Solid and open dots are the results of Wang *et al.* [61] and Csiszar *et al.* [5], respectively. Values obtained from own LEED *I(E)* experiments are shown by solid squares as a function of thickness. The vertical error bars represent the the accuracy of the kinematic approach from reference [66]. The solid line is a guide to the eye. Dashed and dashed-dotted horizontal lines represent the interlayer spacing value for bulk CoO and Ag(001), respectively.

the energy of these peaks is visible when going from Ag(001) to CoO/Ag(001). The square of the momentum transfer vector is proportional to the Bragg peak energy position thus a shift of the peaks to lower values corresponds in real space to an increase in the length scale, here to an increase in the layer spacing. Figure 4.5 (b) shows the linear regression of the energy peak position versus n^2. The vertical interlayer spacing was obtained as explained in Sect. 3.2.2. The value used for the inner potential was $U_0 \approx -10 \pm 0.5$ eV. The inner potential value used for the "best" fit model by Wang *et al.* for CoO/Ag(001) was –9 eV [61]. In the figure, a small increase in the slope for 7 ML CoO compared to clean Ag(001) is the visible.

Figure 4.6 shows the thickness dependence of the interlayer spacing for the CoO thin films on Ag(001). The interlayer distance seems to increase with the thickness, but this trend might not be real. The origin of this effect can be found in the finite probing depth of LEED which gives wrong values for small

layer coverage, because the kinematic approach yields an average value of the top 3–4 ML. For a thickness of more than 6–7 ML CoO, when the substrate contribution can be neglected, the interlayer spacer value tends to be constant. The analysis yields an increase from $a/2 = 2.13$ Å for bulk CoO to $a/2 = 2.17$ Å in thin film range for thicknesses more than 6 ML. For comparison, values from two different references are added to the graph. The interlayer spacing value of Ag(001) yielding form the LEED $I(E)$ measurements is $a/2 = 2.052$ Å which is very close to the bulk interlayer distance for Ag(001) ($a/2 = 2.045$ Å).

The vertical distortion of the CoO film deposited on Ag(001) will play an important role in this work as will be explained in the following sections.

4.2   Macroscopic magnetic properties - Kerr effect

This section presents the results of the magnetic characterization of Fe/CoO bilayer systems studied by magneto-optical Kerr effect (MOKE).

One of the few experimental methods that can address directly the antiferromagnet is neutron scattering, but this needs a neutron source and relatively thick films). Therefore, MOKE magnetometry of an adjacent ferromagnetic layer is a very popular indirect method to probe the antiferromagnetism of thin layers. As presented in Sect. 2.1, under certain conditions (*i.e.* zero-field-cooling or field-cooling), the magnetic coupling in a FM/AFM system manifests itself in an increase in the coercive field H_C (and a shift along the field axis for field-cooled samples).

In longitudinal geometry, the sample was rotated about the surface recording the corresponding FM hysteresis loops for different angles. The easy axis of the FM was found to be along the $\langle 110 \rangle$ crystallographic directions of the substrate. No signal was found employing the polar moke method, which is sensitive to the out-of-plane component of the magnetization. Figure 4.7 presents the hysteresis loops for 5 ML Fe/ 6.5 ML CoO/Ag(001) measured at different temperatures. The increase in the coercive field as temperature decreases is an indication of the appearance of FM/AFM coupling. The 300 K loop is the Fe signal when the CoO is in the paramagnetic state and has no influence on the ferromagnetic layer.

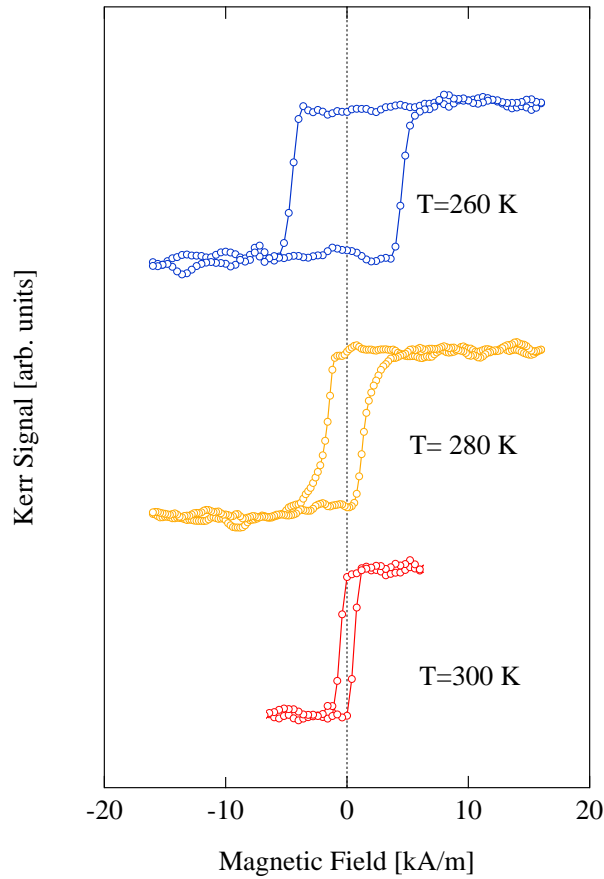Figure 4.8 displays the MOKE results for a series of continuous CoO

Figure 4.7: Hysteresis loops for 5 ML/6.5 ML CoO/Ag(001) recorded for different temperatures below and above the Néel temperature of CoO. The external magnetic field was set along the [110] direction of the substrate. The increase of the coercive field is an indication of the paramagnetic-antiferromagnetic phase transition of the oxide layer. The system was cooled down in zero field, thus no shift in the field is visible.

films with increasing thickness having on top 6 ML Fe. A big increase in the coercive field is visible for thicknesses above 8 ML CoO. The different slopes of the lines in the graph can be understood as a thickness dependence of the coupling strength between the two magnetic layers. The onset of the coercivity enhancement represents the ordering temperature of the antiferromagnetic CoO. A discontinuity in the slope of the lines in Fig. 4.8 indicates a magnetic phase transition in the antiferromagnetic layer. Clear discontinuities at the temperature indicated by T_{AFM} are observed for 8 and 10 ML and less clear for lower thicknesses of CoO. The measurements were done close to the Néel temperature of bulk CoO and show that this remains the ordering temperature of the oxide film, as well.

It was also checked for a possible ferromagnetic order in a pure CoO film without Fe overlayer due to a possible Co cluster formation or ferromagnetism at the film surface or film-to-substrate interface. A reorientation of the magnetic spins was excluded from the start since the external magnetic field
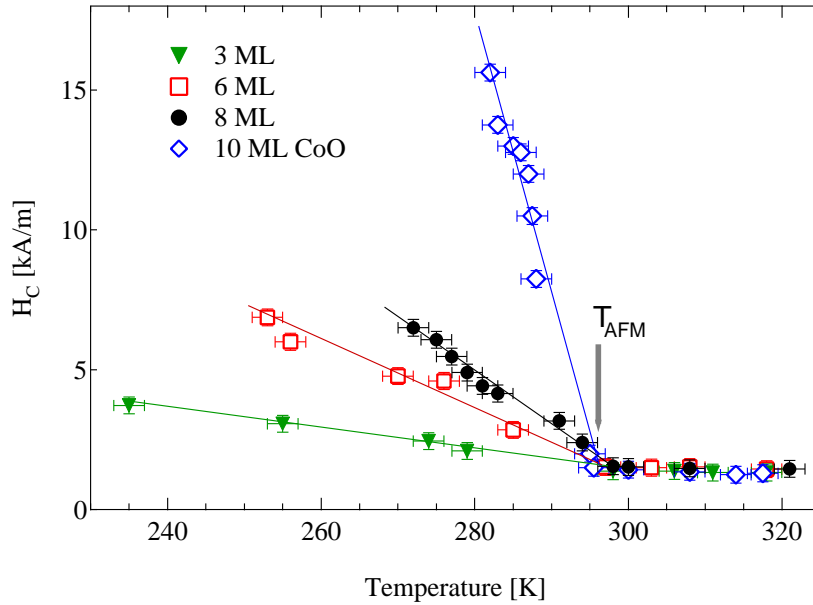
Figure 4.8: Thickness dependence of the coercive field (H_C) in the vicinity of the sup-posed magnetic phase transition of the aniferromagnet (T_{AFM}). The onset of the coer-civity enhancement is related to the ordering temperature of the AFM layer. The solid lines are guides to the eye.

was not strong enough to saturate the oxide layer. For a single CoO film, no MOKE signal was detectable in neither perpendicular nor longitudinal geome-tries. However, as it will become clear in the next sections, a small ferromagnetic net moment related to Co atoms at the interface can be present in the Fe/CoO bilayers.

4.3   Magnetic spectroscopy

This section contains the spectroscopy results obtained for a single CoO film and for Fe/CoO bilayers measured in magnetic remanence. Spectroscopic char-acterization of both layers, as well as of the interface, is presented.

4.3.1   Measurement geometry

To address each layer separately, the X-ray energy was tuned to the Fe and Co $L_{2,3}$ edges. Different measurement geometries were established in order to

reveal the electronic and magnetic properties of both ferromagnetic and antiferromagnetic layers. Figure 4.9 shows the two main geometries employed in this work for measuring the circular and linear dichroism.
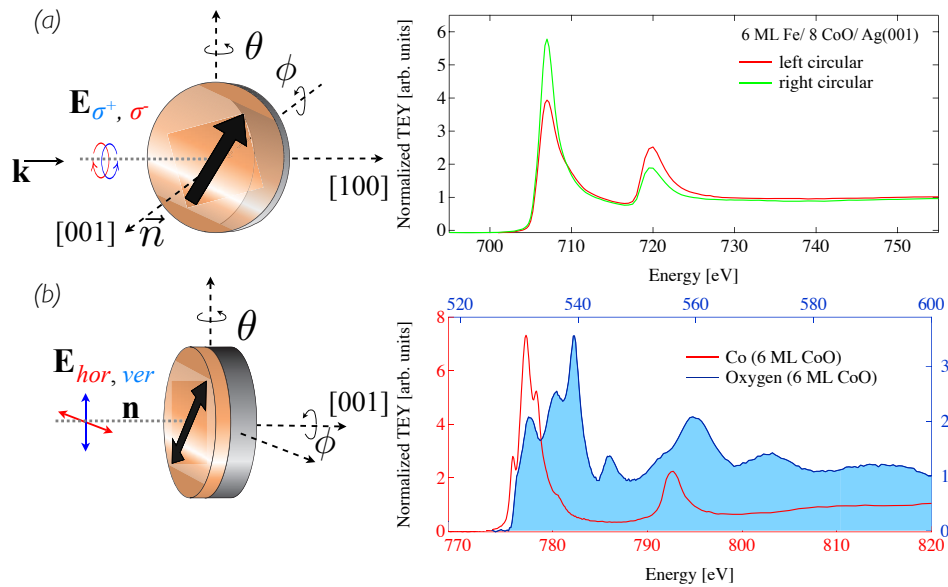

Figure 4.9: Measurement geometries used in this work for the spectroscopy experiments. In the first case (a), the XMCD signal is measured in grazing incidence with an angle θ between the incoming X rays and the vector normal to the surface. For a short characterization of the ferromagnetic layer, two Fe spectra for different photon polarization are presented as an example. This geometry allows to probe the magnetic properties of ferromagnetic layers. In the second case (b), the geometry is changed to normal incidence. We have used this geometry to probe the antiferromagnetism of the CoO layer. As an example, spectra for both constituents of the CoO are presented here. Co and oxygen spectra were measured with horizontally polarized light at normal incidence for 6 ML CoO/Ag(001). Different energy scales for Co and oxygen are here depicted in red and blue colors. All the spectra in the graph were normalized to zero and one in the pre-edge and post-edge region, respectively. This alignment makes it possible to address directly the magnetic properties of the antiferromagnet. As it can be seen in the next sections, for a good overview on the magnetism of the bilayers, combinations between the sample incidence geometry and the light polarization were used.

In both geometries, two important angles were varied to probe directly the direction and orientation of the magnetization in the ferromagnetic and the antiferromagnetic layers. The angle θ (in this work referred as *polar*) is the rotation angle along an in-plane direction of the sample making possible the ro-

tation from normal incidence to left and right grazing incidence with respect to the incoming synchrotron light. This is the angle between the magnetization vector **M** plane and the incoming wave vector **k**. The angle ϕ (referred as *azimuth*) is the rotation angle along the normal to the sample surface as shown in Fig. 4.9 and represents the angle between the [100] direction and the horizontal **E** vector. Concluding, this represents the angle between projection of the magnetization vector **M** on the sample plane and the incident wave vector **k**. Finally, the measurement geometries were dubbed polar and azimuthal.

The ferromagnetic properties of Fe and CoO layers were studied using the alignment described in Fig. 4.9 (a). A circularly-polarized incoming synchrotron X-ray beam impinged the sample at grazing incidence determined by the polar angle θ, in order to address the in-plane magnetization of Fe. Unless indicated, all the XMCD data in this work were recorded at $\theta = 70°$. As an example, two intensity spectra at the Fe $L_{2,3}$ edges recorded for both circular polarization are presented.

To investigate of the antiferromagnetism of the CoO layer, the geometry was changed from grazing to normal incidence by the polar angle θ (b). In this geometry, the linearly polarized X rays probe now the CoO spin axis. The reason to adopt this geometry will be revealed in the next sections. As an example, the characteristic Co and oxygen spectra recorded with linearly polarized X rays at $\phi = 0°$ are presented in the figure.

4.3.2 Single CoO film

A 10 ML CoO film was prepared by following the recipe described in Sect. 3.1. The sample was characterized using AES and LEED prior to the XAS experiments.

In order to determine the effect of the crystal structure on the linear dichroism, XLD spectra were acquired at $T > T_N$ for 10 ML CoO/Ag(001). The spectra were recorded varying the polar angle from $\theta = 0°$ (normal) to $\theta = 70°$ (grazing) [see Fig. 4.10 (a)]. The different shape of the spectra [Fig. 4.10 (a)] is attributed to the breaking of the cubic symmetry originating from the vertical lattice expansion of the film due to the lattice mismatch between CoO and the Ag(001) substrate as found by LEED *I(E)*. The dashed curve in the figure represents the difference between the two absorption spectra recorded at normal incidence and grazing incidence, while keeping the azimuth angle at the same
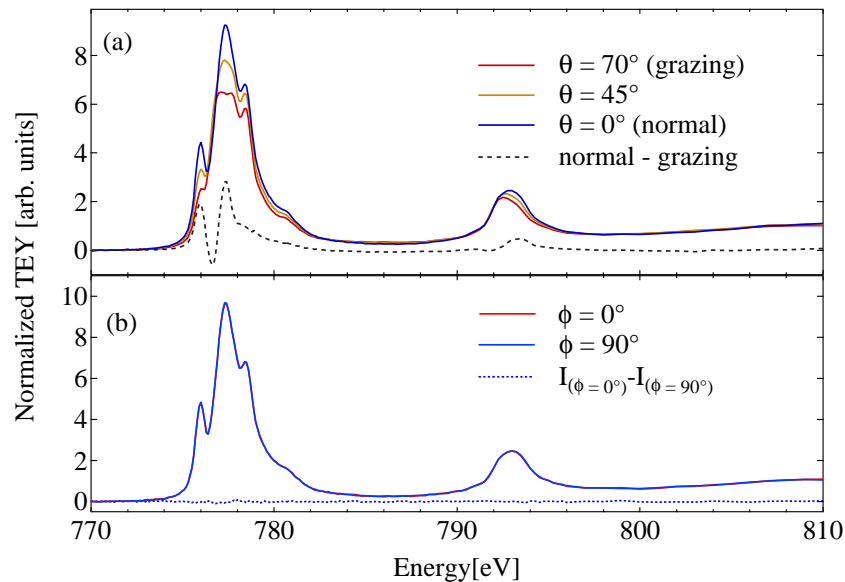
Figure 4.10: Polar angle dependent X-ray absorption spectra (XAS) for epitaxial 10 ML CoO/Ag(001) at room temperature (a). A structure-related linear dichroism occurs in both Co $L_{2,3}$ edges and is evident in all the oxide spectral features of the L_3 edge absorption peak. (b) The azimuth angle was changed from $\phi = 0°$ to $\phi = 90°$ at normal incidence ($\theta = 0°$). ϕ represents the angle between the [100] crystallographic direction of the substrate an the horizontal **E** vector.

value $\phi = 0°$.

When going to normal incidence and varying the azimuth angle from $\phi = 0°$ to $\phi = 90°$, no dichroism was found [Fig. 4.10 (b), dotted line]. The reason for this is a perfect crystallographic fourfold in-plane symmetry of the CoO film for this thickness range. The dotted line in the panel (b) is the difference between the two spectra recorded for $\phi = 0°$ and $\phi = 90°$ at normal incidence ($\theta = 0°$).

Figure 4.11 (a) shows a zoomed-in image of the Co L_3 edge of the spectra presented in Figure 4.10 for normal and grazing incidence, normalized to the same maximum for a better comparison. The linear dichroic signal appears in all the spectral features of the L_3 edge absorption peak: at 776 eV (close to the pre-edge), 777.3 and 778.4 eV (on the resonance peak, L_3) and 780.5 eV (post-edge).

For normal incidence, two different spectra were recorded for room and for low temperature ($\approx$150 K). Fig. 4.11 (b) shows the L_3 edge for 10 ML CoO.
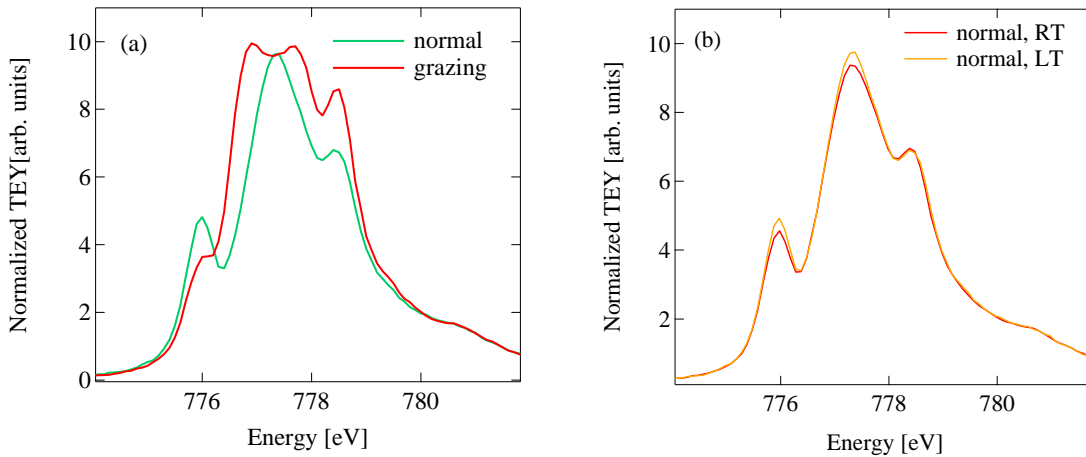
Figure 4.11: Oxide features at L_3 edge for CoO (from Fig. 4.10) for two different sample alignment to the incoming synchrotron radiation due to the so-called "search light effect" (a). For better comparison, both spectra are normalized to the same maximum. (b) Spectra recorded at 300 K and 150 K for a normal incidence geometry.

There is no major difference between the two spectra at different temperature and the small intensity differences visible in the oxide features at 776 and 777.5 eV are maybe due to a possible misalignment caused by mechanical drift when changing the sample temperature.

The huge linear dichroism found at room temperature for grazing incidence and the absence of dichroism at normal incidence was the reason for choosing normal incidence to address the *magnetic* linear dichroism. In this geometry, any linear dichroism occuring when rotating the light polarization by 90° has to be attributed to the magnetism of the sample, as one can see in the next sections.

4.3.3 Fe/CoO bilayers

Fe layer characterization

For 6 ML Fe/10 ML CoO, the XMCD signal at room temperature was measured in order to prove the in-plane orientation of the Fe magnetization.

Figure 4.12 (b) shows the polar angle dependence of the magnetic signal measured at the Fe $L_{2,3}$ edges. Maximum XMCD was found for the maximum reached grazing angle, thus clearly showing that the Fe moments have an in-
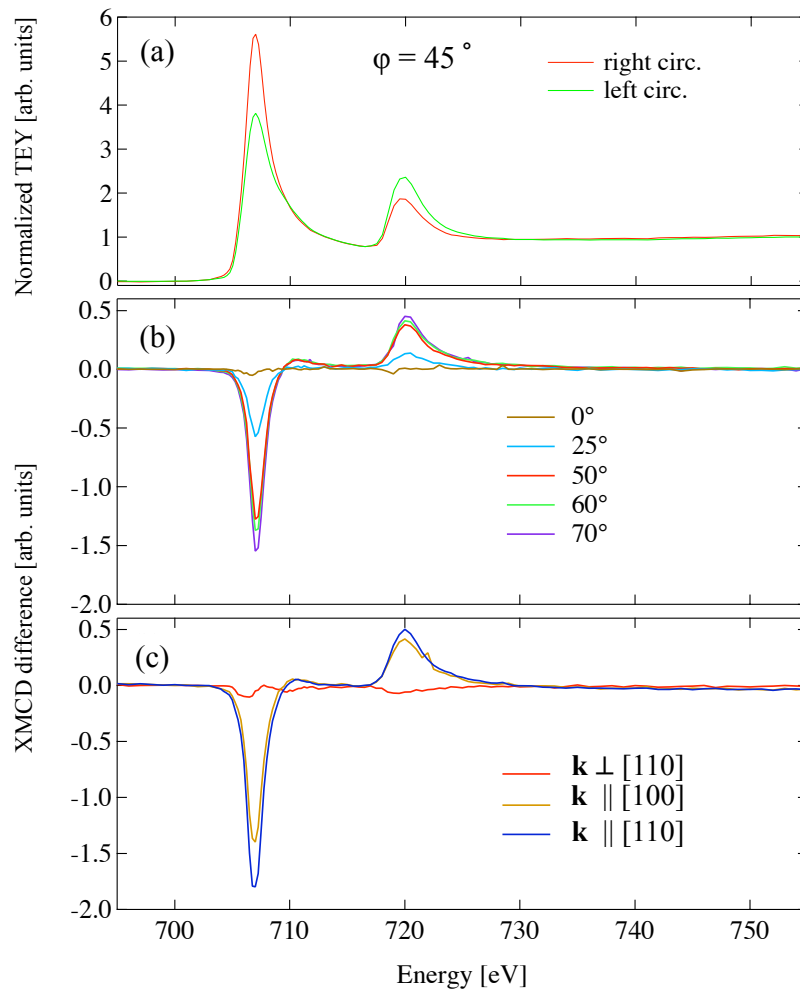
Figure 4.12: Polar and azimuth angle dependence of the XMCD signal measured at the Fe $L_{2,3}$ edges after saturating the sample along [100] direction of the substrate. (a) Two XAS spectra for $\theta = 70°$ and $\phi = 45°$ for opposite X-ray helicities. (b) XMCD signals recorded by varying the polar angle θ from 0°to 70°keeping same $\phi = 0°$. (c) XMCD signal for different azimuth angles ϕ and $\theta = 70°$. The relative orientation with the crystallographic directions is indicated. Measurements were carried out at room temperature.

plane orientation. For a normal incidence of the incoming X rays, the signal extincts as can be seen in figure for $\theta = 0°$. The azimuth angle in this case was $\phi = 0°$. Prior to the measurements, the sample was saturated in an external magnetic $H \approx 400\,\text{Oe}$ along the [100] direction of the substrate, the corresponding XMCD spectra being recorded in magnetic remanence.

At the maximum grazing angle that could be accessed (in our case

$\theta = 70°$), the azimuth angle dependence of the XMCD spectra was recorded. Figure 4.12 (c) shows the XMCD signal for the main crystallographic directions. Maximum signal was found for **k** ∥ [110] and is it decreasing when moving to **k** ∥ [100], and eventually becomes zero for **k** ⊥ [110]. The figure depicts the way that XMCD can be used in a simple manner to find the magnetization of a ferromagnet. In our case, the conclusion of the study is in perfect agreement to the MOKE measurements and shows that the Fe layer, deposited on a CoO film and measured at room temperature, in remanence has the magnetization in-plane, following the [110] crystallographic direction of the substrate.

Structural and magnetic contribution to the XLD signal

We now turn our attention to the spin structure of the AFM CoO film in a 8 ML Fe/10 ML CoO/Ag(001) sample. Prior to the measurements, the bilayer system was saturated in an external magnetic field along the [110] direction as stipulated in Sect. 3.2.5. Figure 4.13 shows the XLD signal measured at different azimuth angles and normal incidence. As can be seen in the figure, the dichroism is visible at both the L_3 and L_2 edges. The measured signal shows a prominent angular dependence at all major features of the L_3 edge, but also at the L_2 edge.

We focus now on the difference signal for 0° and 90° as well as for 20° and 110°. There is a change in sign for the spectra at 90° and 110°, as can be clearly seen at the L_2 edge, but not a perfect reversal with respect to the zero line. A small difference between the "positive" and "negative" XMLD signals is visible. This leads to the conclusion that there is still a small structural contribution included in the overall XMLD. This small structural contribution can be explained by a small misadjustment of the normal incidence angle. In conclusion, in order to get the pure magnetic signal from the total dichroic signal, a separation of these two contributions has to be carried out.

The separation of the overall XLD signal in a magnetic and a structural part was done in two steps. In the first step, the orientation of the antiferromagnetic spin axis was determined by looking at the sign reversal of the XMLD signal for different ϕ angles. For the beginning, a number of ten different energies E_i were selected. The energies were chosen at the L_3 and L_2 edges in a way that for each energy, the function $I_{XLD}(E_i, \phi)$ shows a strong angular dependence. The total XLD signal I_{XLD} was plotted as a function of ϕ, where ϕ
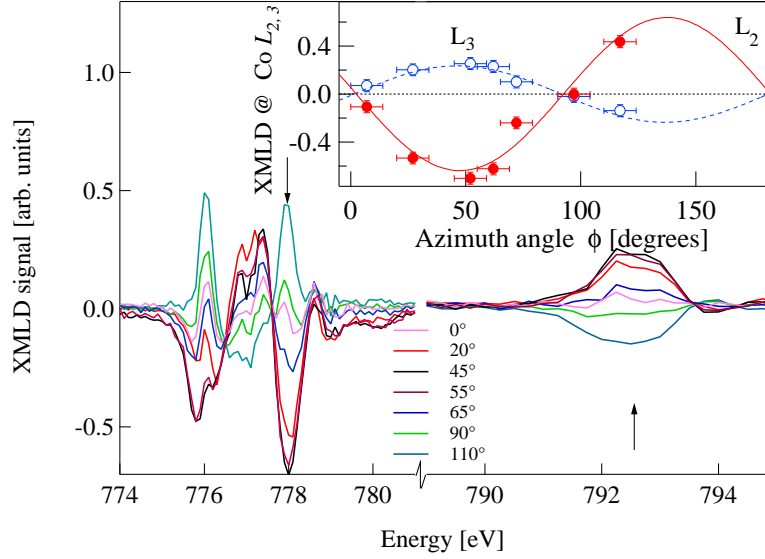
Figure 4.13: Azimuth dependent XMLD for 6 ML Fe/10 CoO/Ag(001) at 150 K. The curves are the difference between their respective XAS spectra recorded at normal incidence with horizontal and vertical linearly polarized light. Inset shows the L_3(778 eV) and L_2(792.5 eV) maximum as function of the azimuth angle. The data was fitted with a $\cos 2\phi$ function.

takes the values shown in the graph. The inset of Fig. 4.13 shows as an example the data points for $E_i = 792.5$ and 778 eV. Each of the ten data points was fitted with:

$$I_{XLD}(E_i, \phi) = a(E_i) + m(E_i) \cos 2(\phi - \delta_i), \tag{4.1}$$

yielding ten values including their standard deviations for the free fitting parameters a, m, and δ_i. From these, one can calculate the average phase $\bar{\delta}_i = 1.2°$, by weighting the δ_i values with their corresponding inverse standard deviation $1/\Delta\delta_i$. In order to obtain the magnetic $m(E_i)$ and the structural (artefact) $a(E_i)$ contribution, the $I_{XLD}(E_i, \phi)$ fitting was applied to all the energies E_i where $E_i = 770, \dots, 810$ eV and keeping the phase constrained to its averaged value $\bar{\delta}_i$.

The result is shown in Fig. 4.14. The error bars in panel (a) and (b) are given by the standard deviations of $a(E_i)$ and $m(E_i)$ as obtained from the fit. The XMLD spectrum in (a) represents the magnetic contribution on the measured XLD. It exhibits a negative–positive–negative sequence of peaks at the L_3 edge. The shape resembles with the ones published in [106]. Figure 4.14 (b) and (c) show as a direct comparison the residual artefact $a(E)$ and a measured
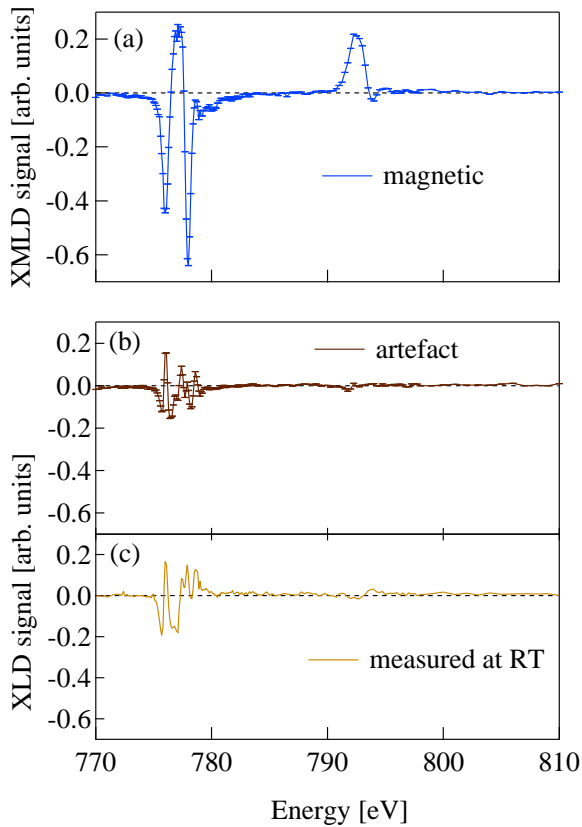
Figure 4.14: Separation of the magnetic ($m(E_i)$) and structural ($a(E_i)$) contribution at the overall XLD signal. Panel (a) shows the pure magnetic signal. For comparison the residual structural signal after separation (b) and the measured dichroic signal for CoO at $T > T_N$ (c).

XMLD spectrum for same sample for $\phi = 45°$ at room temperature, when the magnetic contribution to the dichroic signal is zero. As can be seen, the two signals resemble each other in magnitude and also in shape, thus supporting the success of the separation method used, which can be an useful tool to discover the real magnetic part for an X(M)LD signal.

Another way to check whether the measured signal is exclusively due to the magnetic signal of the CoO is to perform temperature-dependent XMLD experiments. These are one of the most time consuming experiments since the temperature has to be tuned and kept constant during the recording of the spectra, and the sample has to be realigned for each temperature. The results are presented in Fig. 4.15 for different temperatures. The magnetic signal at 150 K has the same shape as determined by separating the two contributions at the XMLD signal, and is nearly vanishing when heating the sample up to room temperature. The inset of Fig. 4.15 depicts the temperature dependence of the XMLD signal at an energy where the structural part is minimum. The remaining signal (the curve at RT) represents the structural part of the dichroic signal, mainly due
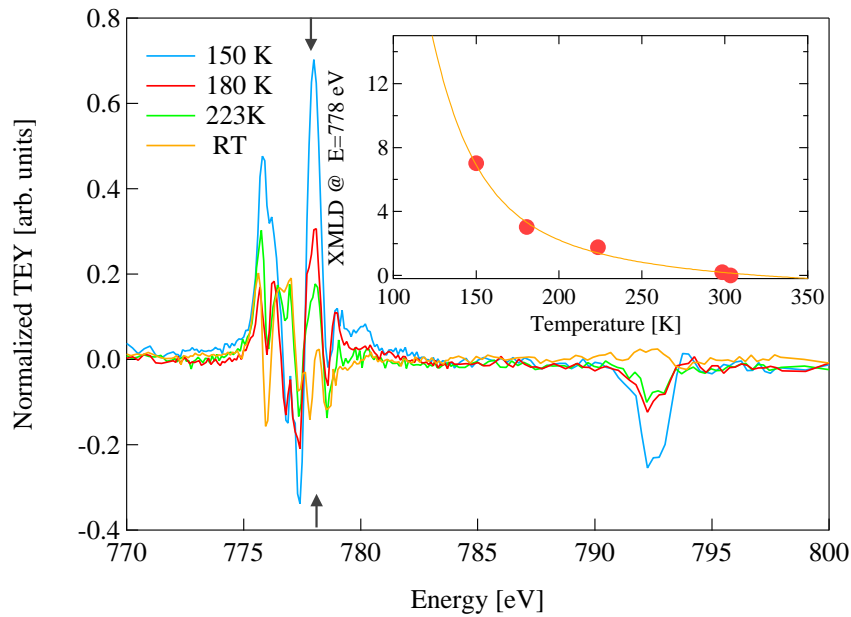
Figure 4.15: XMLD temperature-dependence measured for 6 ML Fe/ 10 ML CoO at $\phi = 45°$. The signal recorded at low temperatures diminished when heating up the sample to room temperature. This is the indication of a magnetic dichroism in the CoO film. As an example, the inset shows the decay of the 778 eV L_3 peak as function of temperature. In addition, a contribution due to a possible misalignment of the sample which remains at room temperature is also observed. For convenience the spectra were multiplied by (-1).

to a possible misalignment of the sample. As can be seen in Fig. 4.14 (b, c), the structural part of the overall XMLD signal is very small and its main features can be found at the energies where the magnetic part has also a large amplitude – the magnetic and structural parts are overlapping in the main peaks of the L_3 and L_2 edges.

    For the next set of samples measured in the next beamtime, the substrate alignment was readjusted in order to reduce the structural dichroism contribution, so that the measured XMLD spectra represent only the pure magnetic signal.

Magnetic coupling between Fe and CoO

In the next step, the XMLD spectra of a 6 ML Fe/10 ML CoO/Ag(001) sample was measured after applying a magnetic field of 400 Oe along the [110] sub-
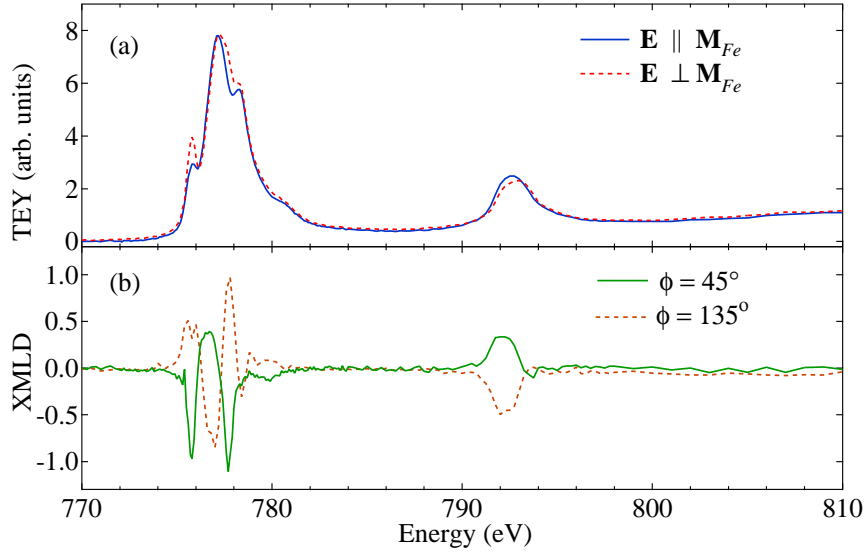
Figure 4.16: (a) X-ray absorption spectra for 6 ML Fe/10 ML CoO/Ag(001) bilayers at the Co $L_{2,3}$ edges recorded with linearly polarized light. (b) difference between this two spectra gives their corresponding XMLD signal for $\phi = 45°$. The dotted line is the dichroic signal corresponding to the second set of absorption spectra (not shown here) recorded for $\phi = 135°$.

strate direction (thus saturating the Fe layer) and then cooling down to 150 K. Figure 4.16 (a) shows two Co $L_{2,3}$ XAS spectra measured with the **E** vector of the incoming light parallel to the [110] substrate direction (full line) and perpendicular to it (along [1$\bar{1}$0], dashed line). The azimuth angle of the sample was in this case $\phi = 45°$. Panel (b) shows the XMLD signal obtained as the difference of the above spectra (full line), and comprises a succession of sharp negative/positive/negative peaks at 775.8, 776.6 and 777.7 eV (L_3 edge) and a single broader positive peak centered around 792.0 eV (L_2 edge). The asymmetries for these energies, defined as $A = \frac{I_v - I_h}{I_v + I_h}$, are -14.1, 3.8, -8.8 and 7.0%, respectively. All the spectral features found in the XAS and XMLD lineshapes are in good agreement with literature results on CoO(8 ML)/NiO(100) [107], where no in-plane or out-of-plane lattice distortion was observed. We also present in Fig. 4.16 (b) the XMLD spectrum for $\phi = 135°$ (dashed line). Apart from the sign reversal, all the features found for $\phi = 45°$ are reproduced.

By following the maximum Fe L_3 XMCD and the maximum Co L_2 XMLD signals as a function of ϕ, we are able to probe the evolution of the Fe magnetization *vs* temperature and the magnetic coupling of the two layers. Fig-
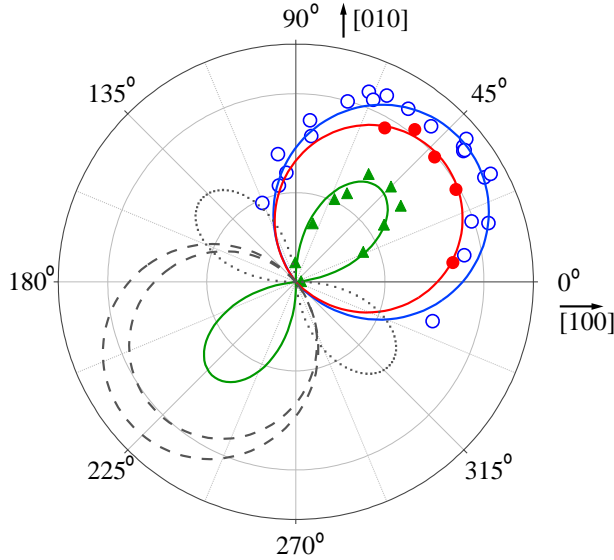
Figure 4.17: Azimuth dependence of the XMCD and XMLD signals. Full and open circles represent the Fe L_3 XMCD signal at room temperature and at 150 K, respectively; full triangles represent the measured Co L_2 XMLD signal at 150 K (5×). Lines are data fit with the respective trigonometric function as described in the text.

ure 4.17 shows a polar plot of the Fe L_3 XMCD (dots) and Co L_2 XMLD (triangles) signals *vs* ϕ measured at grazing and normal incidence, respectively. The open and solid symbols represent data taken at 300 K and 150 K, respectively, and the XMLD signals were multiplied by a factor of five for a better view. The lines show best fits of the XMCD and XMLD data to $a \sin(\phi + \phi_{Fe})$ and $b \sin[2(\phi + \phi_{Co})]$ functions, respectively, where a and b are constant scaling factors. From the fitting of the Fe XMCD at 300 K, an angle $\phi_{Fe}(RT) = 44.3°$ between $\mathbf{M}_{Fe}$ and the [100] axis is obtained, as expected. After zero-field cooling, the Fe magnetic easy direction is kept ($\phi_{Fe}(LT) = 42.5°$), agreeing within the error with the MOKE results described in Sect. 4.2. However, a small decrease in the XMCD intensities is observed, which can be explained by a partial breaking-up into domains or by a local canting of the Fe magnetization concomitant to the development of the CoO antiferromagnetic order.

Furthermore, the azimuthal dependence of the XMLD signals leads to a 47.9° angle between the CoO spins and the ⟨100⟩ crystal directions. In the figure, the broken lines means an opposite sign for XMLD and XMCD signals.

Chemical reactions at the Fe/CoO interface

One can intuitively expect that the interface between a metal and an oxide is not sharp. For a complete description of the interface, chemical effects have

to be considered. The electronegativity of these two species (Fe and Co) is the property which controls the interface formation from the chemical point of view. Electronegativity is the measure of electron acceptance – lower electronegativity means that the presence of oxygen can lead to a higher oxidation factor. The inverse effect is reflected in the reduction factor. Hence, an interface between an oxide and a metal may be characterized by oxidation–reduction effects. The oxidation (reduction) values for Fe and Co are 1.6 (-0.47 V) and 1.7 (-0.27 V), respectively [108]. Using this, one can conclude that the Fe can reduce the CoO, leading to an oxidation of the metallic layer.

To check whether such oxidation–reduction reactions occur at the Fe/CoO interface, different thicknesses of Fe were deposited on a freshly pre-pared CoO film. Figure 4.18, shows different thicknesses of Fe layer deposited on the 8 ML CoO/Ag(001) starting from some fractions of a monolayer, in order to probe the chemical state of the ferromagnet at the interface. Deposition and measurements shown here were done at RT. Each Fe XAS spectra was recorded immediately after deposition so that ferromagnet-to-vacuum interface oxida-tion can be excluded. Small thicknesses of Fe on top of the CoO were used to allow the detection of small chemical effects at the interface.

The only evidence of Fe oxidation can be seen in the spectrum for 0.5 ML Fe [inset of Fig. 4.18]. A direct comparison with the results obtained by Regan *et al.* [4] suggests the existence of some oxidized Fe that has a structure close to the FeO–type.

In the inset, the arrows emphasize the oxidation shoulders which occur at the same energies as in the FeO; the formation of Fe_3O_4–type oxide can be excluded, since the energy shift in the L_3 edge present in the Fe_3O_4 spectra here is not evident. The energy shifts of the L_3 peak maximum were experimentally determined to be ~ 0 eV for FeO, and ~ 1.4 eV for Fe_3O_4 [109].

Interfacial uncompensated magnetic moments

One of the characteristics of a FM/AFM bilayer system is the interfacial induced magnetic moments in the antiferromagnet – the FM material may induce an or-der into an AFM in the first few layers near the interface. In this way the in-terfacial antiferromagnetic spins might be aligned with the ferromagnetic ones nearby.
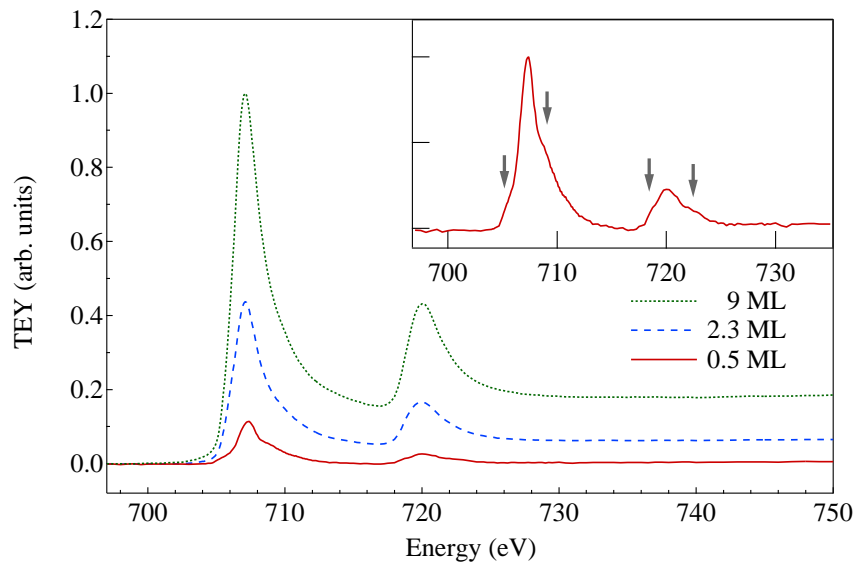
Figure 4.18: XAS spectra for different thicknesses of Fe deposited on 8 ML CoO/Ag(001). The inset shows the zoomed-in spectra for 0.5 ML Fe/8 ML CoO/Ag(001); oxidic features emphasized by the arrows indicate the FeO–type of oxide. Since there is no peak shift in the Fe L_3 edge maxima, Fe_3O_4 –type of oxide formation can be excluded. Weak oxidation features are expected for FeO [4].

In Figure 4.19 (a), XAS spectra of the Co $L_{2,3}$ edges for left and right circular light polarization are presented. Note the presence of a large circular dichroism at the Co L_3 and L_2 edges. Panel (b) shows the difference of the upper spectra (solid line) together with the XMCD signal recorded for 10 ML Co/Cu(001) (dashed line). The metallic Co signal was reduced by a factor of four in order to fit at the L_2 edge and to allow a direct comparison of the L_3 edge. More fine structure is evident in the CoO spectrum than in the Co one. Furthermore all the features in the Co induced moments are replicating the spectral features of the XAS spectra. This leads to the conclusion that the Co at the interface is keeping the oxygen bonding and at the same time, is magnetically coupled to the ferromagnetic Fe layer. Hence, one can exclude a significant reduction of the CoO at the Fe/CoO interface. The formation of a fully metallic ferromagnetic Co layer between Fe and CoO can thus be excluded as explanation for the induced magnetic moments.

No proof of uncompensated magnetic moments was found for a clean CoO thin film. This sustains the idea that any Co magnetic moments that appear after the Fe deposition are definitely an interfacial effect. Figure 4.20 shows
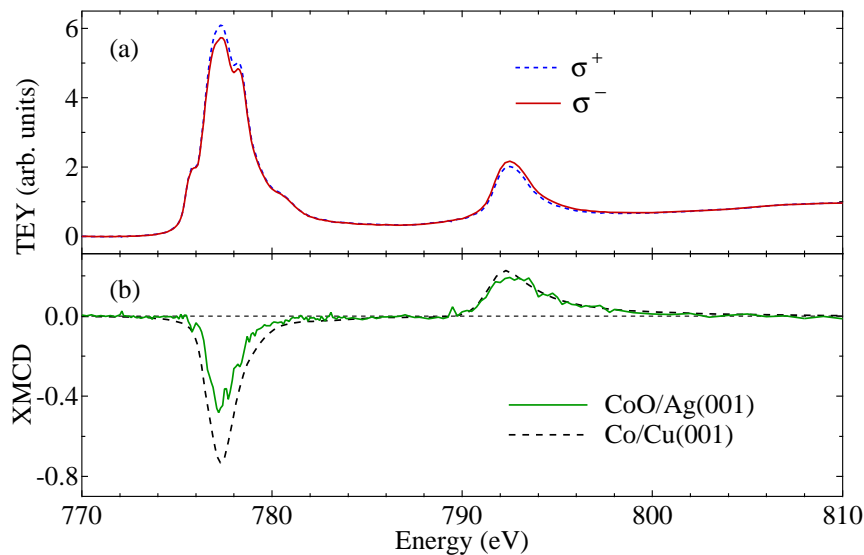
Figure 4.19: XAS spectra (a) and the respective XMCD signals measured at the Co $L_{2,3}$ edges for 6 ML Fe/ 10 ML CoO/Ag(001) (b, solid line) and for 10 ML Co/Cu(001) (b, dashed line). For better comparison of the line shape, the metallic XMCD spectra was reduced by a factor of four in order to fit the oxide spectrum at the L_2 edge. ($\phi = 45°$, T = 150 K)

the XMCD signal measured at the Co $L_{2,3}$ edges for a single 8 ML CoO film (dotted line) and for a 6 ML Fe/8 ML CoO bilayer at room temperature (solid line). Direct comparison between the XMCD signal presented in Fig. 4.19 (b, solid line) measured at low temperatures and the room temperature XMCD in Fig. 4.20 shows no difference, proving that the Co interfacial uncompensated moments are maintained also when the oxide layer does not exhibit AFM order.

A different approach to study the magnetic moments at the interface is to use X-PEEM at the Co $L_{2,3}$ edges, as can be found in the following section.

4.4   Magnetic microscopy

Section 4.2 was presenting the macroscopic magnetic properties of the Fe/CoO bilayer system approaching the antiferromagnet only through the prism of the ferromagnet on top. In order to elucidate the main interactions at microscopic scale, we made use of XMCD-PEEM and XMLD-PEEM. Magnetic domain imaging was performed on Fe wedges deposited on continuous CoO films
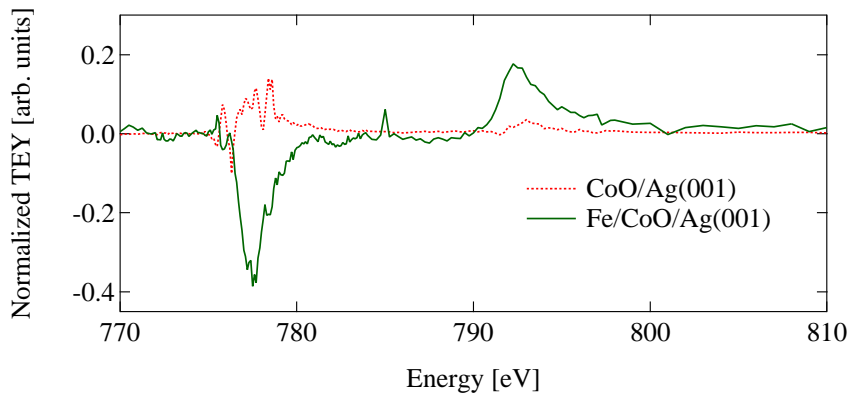
Figure 4.20: Room-temperature XMCD signals measured at the Co $L_{2,3}$ edges. The continuous line represents the XMCD signal recorded from 5 ML Fe/8 ML CoO bilayer system and the dotted line is the signal measured for a pure CoO film ($\phi = 45°$).

on Ag(001). The sample preparation (including here the Fe wedge preparation) was presented in Chapter 3. If for the XMCD images is not needed, due to the big contrast in the asymmetry image, the quality of the XMLD images was improved by increasing the contrast using an scientific image processing software.

4.4.1 Ferromagnetic domains in the as-grown Fe wedge

Figure 4.21 depicts the Fe domain structure along the wedge for an Fe/CoO system. The maximum thickness of the ferromagnetic layer (the thickness in the plateau area) is 8 ML, and the CoO film thickness is 10 ML. The subsequent images were recorded while keeping the field of view close to the sharp edge of the sample and moving from the pure CoO area (contrast-less pictures in the right) to the top of the wedge.

The line profile was recorded from the horizontal profile of the images as $(\mu_{L_3}^+ + \mu_{L_3}^-)/(\mu_{pre}^+ + \mu_{pre}^-)$, where μ_{L_3} and μ_{pre} represent the images recorded at the L_3 edge (707 eV) and before the L_3 edge (699 eV), respectively, for both circular polarization directions of the X rays.

The onset of the Fe layer, indicated by the vertical arrow in the line profile, does *not* coincide with the onset of the magnetism. As expected, from ≈ 2 ML thickness, the Fe starts to be magnetic, this being visible in the PEEM images on the left side of the dotted vertical line. For a better characterization of the wedge, a profile of the sharp edge (blue vertical line) taken at 6.5 ML Fe
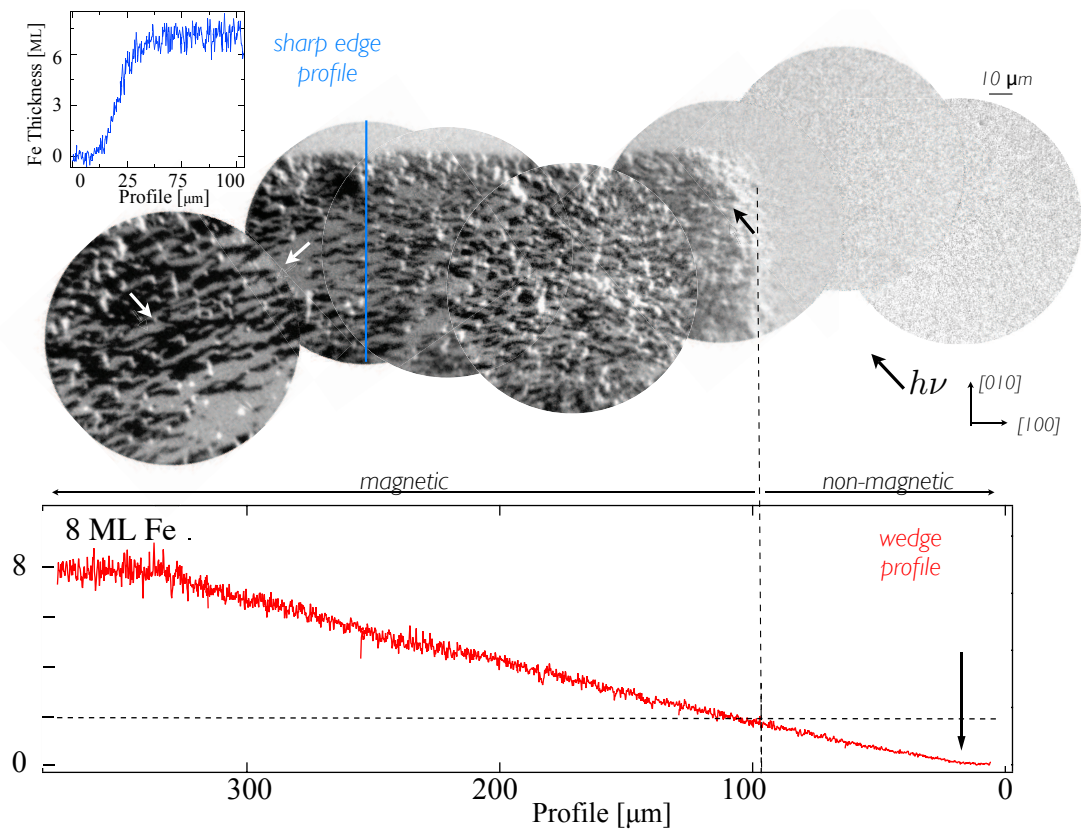
Figure 4.21: Magnetic domain image obtained at the Fe L_3 edge, of an Fe wedge with a plateau level thickness of 8 ML, imaged by X-PEEM. The ferromagnet thickness increases from right to left. The profile presented at the bottom shows the vertical characteristic of the wedge. The onset of the Fe wedge is indicated by the vertical arrow. The onset of magnetism in the Fe layer (dotted line) can be found as the starting point of the magnetic domains in the Fe layer. For a good overview on the geometry of the wedge, a profile scan for the sharp edge along the vertical blue line is also presented.

thickness, is also presented. The domain pattern shows in this case small domains especially in the thin Fe regions, therefore a field of view of $\approx 100\,\mu m$ was used[1].

4.4.2   XMLD-PEEM image formation

The acquisition procedure of the XMLD-PEEM images is slightly different than for the XMCD case. Our experiment makes use of the relatively large XMLD effect presented in the previous section. A linearly-polarized X-ray beam is il-

---

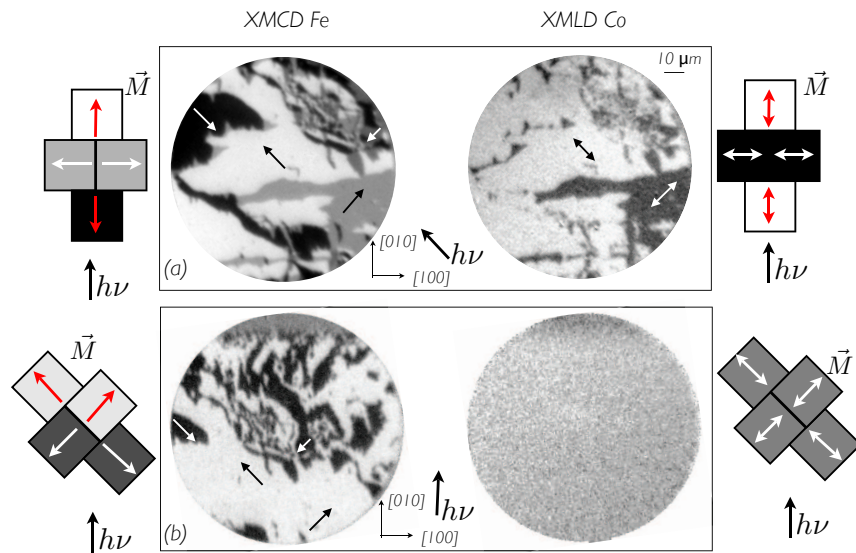[1]The default survey mode has a field of view of 350–500 μm.

Figure 4.22: Ferromagnetic and antiferromagnetic domain formation in PEEM. The images on the left inside represent the ferromagnetic signal for the Fe layer measured at approximately the same sample position for two different incidence angles of the incoming light. Note here the change in contrast, from a four-level contrast in the upper to a two contrast level in the lower picture. The right inside shows the respective XMLD images measured at the Co L_3 edge. Note here the vanishing of the signal in the second case, after the sample was rotated 45°. Measurements were carried out on 8 ML Fe/10 ML CoO/Ag(001) at 170 K. The crystallographic directions as well as the magnetization directions are indicated in the figure.

luminating the sample at an angle of 30° to the surface, with the electric field vector **E** oriented parallel to the surface (*s* polarization). Instead of switching the photon polarization like in XMCD-PEEM, the magnetic contrast is achieved from the asymmetry of two PEEM images recorded at two different energies (777.0 and 777.8 eV), thus exploiting the sign reversal of the XMLD signal for the same linear polarization (in this case horizontal or *s*-polarized). In Fig. 4.22, good examples of image formation in the cases of XMCD and XMLD are presented. For the **k** vector parallel to the [100] direction of the sample, the magnetic contrast in the PEEM image (panel b) for Fe consists of two levels of grey. Because of the fourfold symmetry of the system, this means that the magnetization vector has a 45° angle with the incoming X rays (**k**). In this case, the CoO antiferromagnetic domains have their spins oriented also at 45° with respect to the incoming light, thus the achieved magnetic signal for the antiferromag-
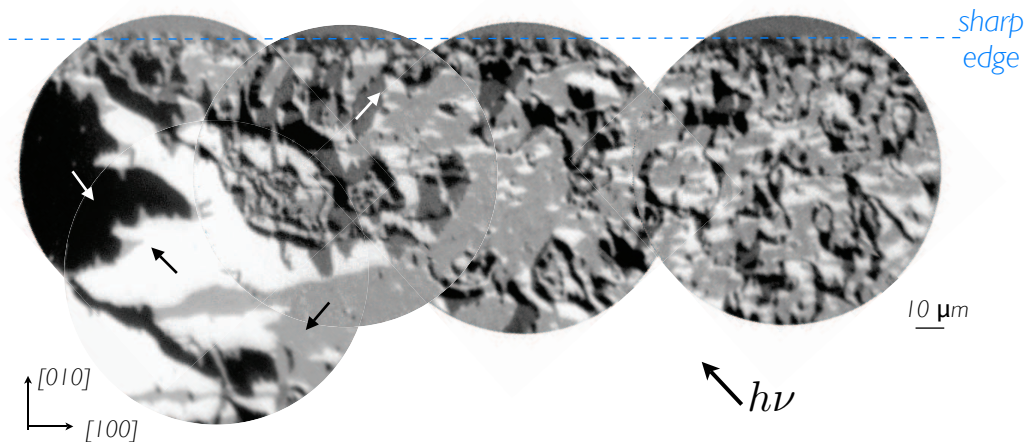
Figure 4.23: Ferromagnetic domain pattern measured at the Fe L_3 edge for 8 ML Fe wedge/10 ML CoO/Ag(001) along the wedge at room temperature. The images were recorded in the area of the wedge where the Fe thickness is $\approx$ 7–8 ML. The arrows in the image indicate the magnetization directions in the ferromagnetic domains. The sharp edge of the Fe wedge is indicated by the dashed line.

net cancels out and the final XMLD picture does not show any type of contrast (right). A 45° rotation of the sample leads to the case depicted in (a). Due to the rotation, the position of the sample is slightly changed but still allows one to locate the domain pattern seen in (b). Four different contrasts are now visible in the case of the Fe layer. The two measurements allow to find out the direction of the magnetization vectors in each magnetic domain as indicated by the arrows in the figure. For this geometry, the XMLD picture reveals a black and white contrast, making possible the observation of the magnetic domains in the CoO. Black and white domains in the XMCD image can be seen in the case of the CoO XMLD in white, while the gray domains of the Fe XMCD image are represented in black. The possible orientations of the spin axis in the antiferromagnetic layer are indicated with double arrows, if one assumes a parallel orientation of the CoO atiferromagnetic spins with the Fe spins.

4.4.3 Separate imaging of the FM and AFM domains

Figure 4.23 shows a collection of PEEM images recorded along the Fe wedge. As the thickness increases from right to left, the Fe layer starts to develop larger magnetic domains, as can be seen in the images in the left part of the figure. The

arrows show the magnetization direction relative to the incoming X rays direction. In order to check the influence of temperature on the domain structure, the sample had been cooled in zero field down to $\approx$170 K.

The image aquisition procedure is very time consuming and a problem which occurs during LT measurements is the thermal drift of the sample position which, at this magnification, can totally damage the image quality. The nitrogen flow induces additional vibrations of the PEEM sample holder. Thus the resulting images are a "compromise" between the exposure time for each helicity and the nitrogen flux used for cooling. Nevertheless, we succeeded in recording sharp pictures even at the Co edge (XMCD and XMLD) where the acquisition time was 10–12 minutes for each light polarization or energy.

We are now turning our attention to the image with the largest magnetic domains in Fig. 4.23 (bottom left) and reproduced in Fig. 4.24 (a). The image for the Fe XMCD was recorded at 170 K. Then the energy was set to the Co L_3 edge recording the Co XMCD image. In this manner, one is able to image the Co uncompensated moments at the interface. All the magnetic domains in this Co XMCD image follow exactly the Fe domain structure presented in image (a). The same magnetization alignment as for the Fe can be found for the uncompensated Co domain pattern, thus showing the pinning of the uncompensated Co spins to the ferromagnetic layer on top. Also measurements at room temperature have been carried out yielding the same result, in perfect agreement to the spectroscopy experiments described in the previous section. After changing the light polarization from circular to linear horizontal and following the acquisition procedure described above, the image in Fig. 4.24 (c) is recorded. The multi-domain structure from (a), characterized by four distinguished gray levels, is mirrored in (c) into a two grey-level domain structure. As mentioned before, due to the nature of the XMLD effect, domains with opposite magnetization give rise to the same gray level in the image. As can be concluded by direct comparison between the XMCD and XMLD images, the black–white domains and gray domains in (a) transform into white and black domains in image (c), respectively. The very complex domain structure with small magnetic domains that appears in the right-upper part of all the images of Fig. 4.24 is developed at a structural defect in the substrate.

In order to check the domain pattern in the oxide layer in more detail, we turned our attention to the area where the ferromagnetic layer is thin or not
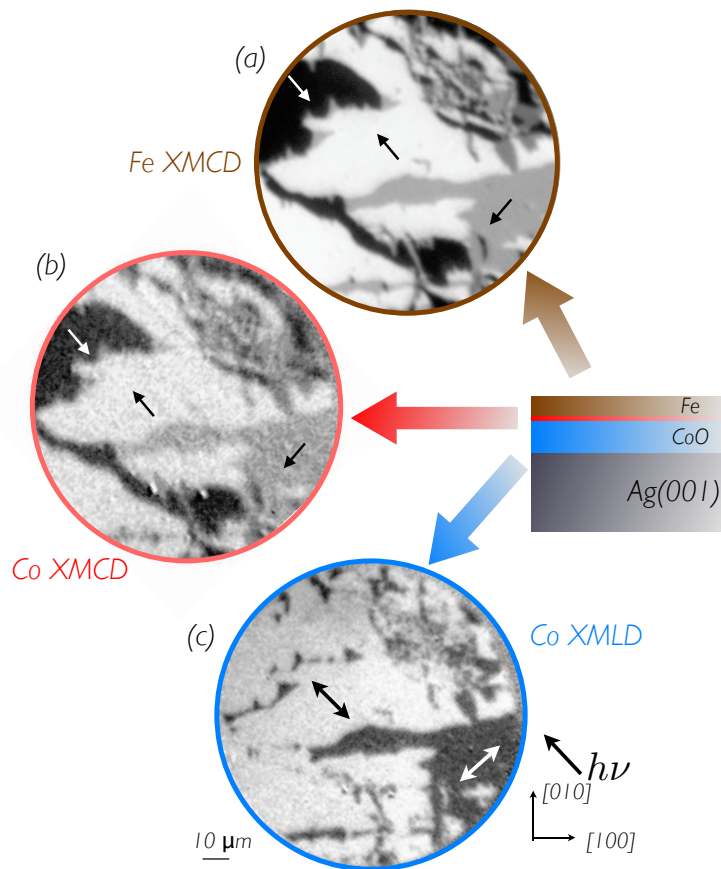
Figure 4.24: PEEM images for 8 ML Fe wedge/10 CoO/ Ag(001) system. The element selectivity of the technique and its magnetic sensitivity lead to the possibility to image each layer separately and, even more, to "break through" at the interface level. The images for Fe (a) and Co (b) XMCD and for Co XMLD (c) signals recorded at the respective L_3 edges at 170 K are shown in different colors for each layer. The direction of the magnetization in the XMCD images and a possible orientation of the spin axes in the XMLD images, as well as the incoming X-ray direction relative to the crystallographic axis are indicated by arrows. Note the coinciding domain structure in (a) and (b), indicating that the induced domain structure at the interface is closely following the magnetization of the ferromagnet. (c) shows only a two different level of grey scale contrast as expected for XMLD in a fourfold symmetry system.
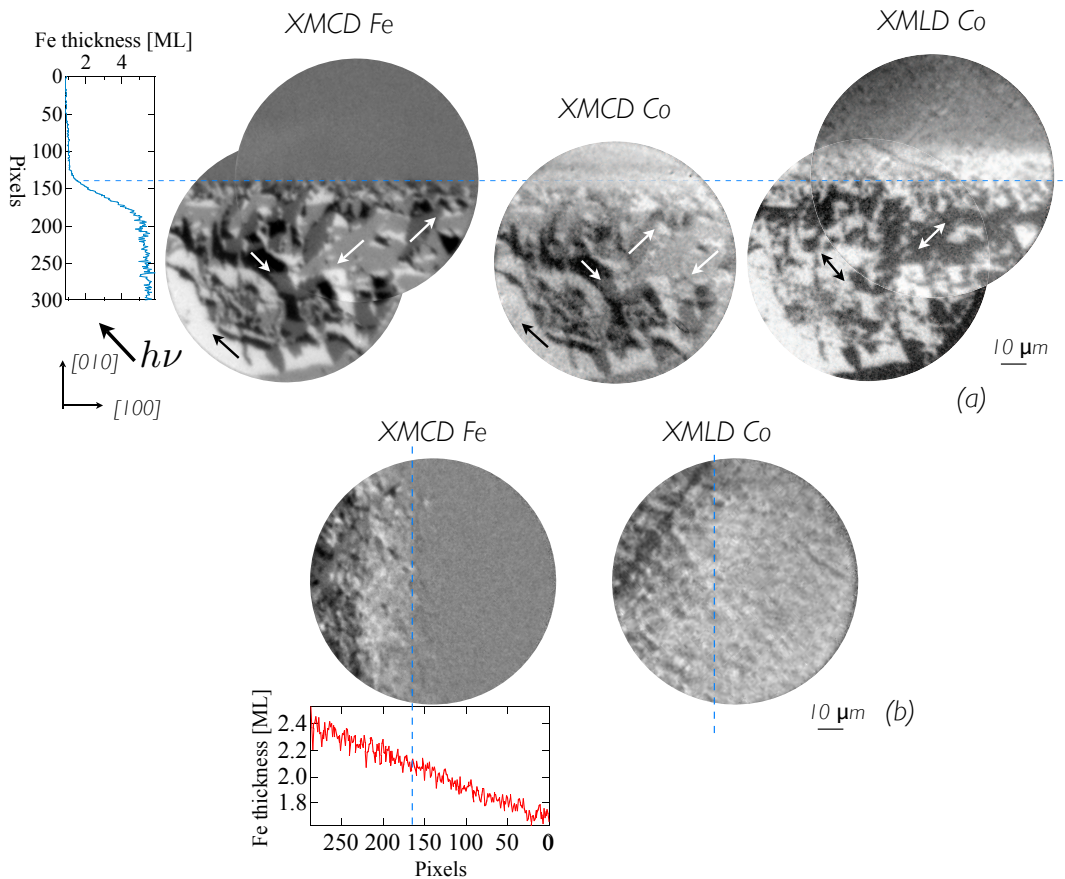
Figure 4.25: XMCD- and XMLD-PEEM images recorded in two different areas of the wedge where the ferromagnet thickness decreases rapidly – close to the sharp edge (a) and gradually – on the wedge (b). Antiferromagnetic domains are still visible in the area where the Fe is not magnetic. The profile plots characterize the Fe layer atop for both cases.

present, and imaged the CoO layer by means of XMLD microscopy.

Hence, the two chosen areas are situated close to the sharp edge of the sample (a) and on the onset of the Fe wedge (b), as can be seen in Fig. 4.25. The line profiles provide a good characterization for the Fe wedge for both positions. The XMCD images for both Fe and Co and the XMLD image for Co are shown in (a) from left to right. A comparison between the XMCD signal at the Fe edge and the XMLD signal at the Co edge reveals a different onset of the domain pattern. The line profile for the edge proves its sharpness but also that it is not perfectly vertical. There is a small amount of Fe that is not magnetic above the horizontal dashed line in (a) because its thickness is less than 2 ML. The

interesting point is that below this non-ferromagnetic Fe one can observe anti-ferromagnetic domains in the Co XMLD image. Moving away from the sharp edge, the magnetic domains are diminished. Nevertheless, antiferromagnetic domains are probably also visible in clean CoO but they may be too small to be resolved, due to the resolution limit of the microscope.

The second area [Fig. 4.25 (b)] was chosen in order to have the onset of the magnetization in the Fe wedge in the field of view. As can be seen from the profile, Fe is present in the entire image, but is not ferromagnetically ordered. The vertical dashed line is the starting point of the magnetism in the wedge. The corresponding XMLD image clearly shows antiferromagnetic domains, also below the non-magnetic Fe layer and their increase in size when moving to the magnetic part of the sample.